J Nanopart Res (2013) 15:1616
DOI 10.1007/s11051-013-1616-3

RESEARCH PAPER

$MZnFe_2O_4$ (M = Ni, Mn) cubic superparamagnetic nanoparticles obtained by hydrothermal synthesis

R. M. Freire · T. S. Ribeiro · I. F. Vasconcelos · J. C. Denardin · E. B. Barros · Giuseppe Mele · L. Carbone · S. E. Mazzetto · P. B. A. Fechine

Received: 17 January 2013 / Accepted: 26 March 2013 / Published online: 7 April 2013

Abstract $MZnFe_2O_4$ (M = Ni or Mn) cubic nanoparticles have been prepared by hydrothermal synthesis in mild conditions and short time without any procedure of calcinations. The structural and magnetic properties of the mixed ferrites were investigated by X-ray diffraction, Fourier transform infrared spectroscopy (FTIR), Raman spectroscopy, Mössbauer spectroscopy, vibrating sample magnetometer, and Transmission electron microscopy (TEM). X-ray analysis showed peaks characteristics of the spinel phase. The average diameter of the nanoparticles observed by TEM measurements was approximately between 4 and 10 nm. Spectroscopy study of the spinel structure was performed based on Group Theory. The predicted bands were observed in FTIR and Raman spectrum. The magnetic parameters and Mössbauer spectroscopy were measured at room temperature and superparamagnetic behavior was observed for mixed ferrites. This kind of nanoparticles can be used as precursor in drug delivery systems, magnetic hyperthermia, ferrofluids, or magnetic imaging contrast agents.

Keywords Mixed ferrites · Magnetic nanoparticles · Hydrothermal synthesis · Cubic morphology

Introduction

Spinel ferrites are important materials due to their structural, magnetic, and electrical properties (Siddique and Butt 2010). For this reason, they have received high attention in the last years for their wide possible applications in the nanostructured materials technology. In the electronic industry, mixed ferrites have been extensively studied. Their high electrical resistivity and excellent magnetic properties make them a good choice (Date et al. 2004). This kind of structure

---

R. M. Freire · S. E. Mazzetto · P. B. A. Fechine (✉)
Grupo de Química de Materiais Avançados (GQMAT)-
Departamento de Química Analítica e Físico-Química,
Universidade Federal do Ceará—UFC, Campus do Pici,
CP 12100, Fortaleza, CE 60451-970, Brazil
e-mail: fechine@ufc.br

T. S. Ribeiro · I. F. Vasconcelos
Departamento de Engenharia Metalúrgica e de Materiais,
Universidade Federal do Ceará, Fortaleza, CE, Brazil

J. C. Denardin
Departamento de Física, Universidad de Santiago de
Chile, USACH, Av. Ecuador 3493, Santiago, Chile

E. B. Barros
Departamento de Física, Universidade Federal do
Ceará—UFC, Campus do Pici, CP 12100, Fortaleza,
CE 60451-970, Brazil

G. Mele
Dipartimento di Ingegneria dell'Innovazione,
Università del Salento, Via Arnesano, 73100 Lecce, Italy

L. Carbone
IPCF-CNR, UOS Pisa, Via G. Moruzzi 1, 56124 Pisa,
Italy

has unit cells containing oxygen ions form close packing (fcc) with spatial symmetry group O_h^7 ($Fd3\ m$) (Vucinic-Vasic et al. 2006). Its general molecular formula can be written as $(A)[B]_2O_4$, where A and B are two non-equivalent symmetrical sites with tetrahedral (8*a*) and octahedral (16*b*) coordination, respectively, occupied by divalent and trivalent cations (Thomas and George 2009). The spinel ferrites have been commercially used for several applications such as radio frequency coils and transformer cores, prepared by the conventional ceramic method involving high temperatures and solid-state reactions, which can result in the loss of their fine particle nature due to the particle growth (Wang and Li 2001; Daniels and Rosencwaig 1970; Leung et al. 1973). However, recent advanced technology demands ferrite particles in nanometric scales before compacting them for sintering (Pathan et al. 2010). For inorganic materials which are normally non-magnetic, its structural defects and compositional variations at surfaces and grain-boundaries of constituent nanoparticles might be responsible for this anomalous magnetic behavior, such as nanotubes ($La_{0.6}Sr_{0.4}MnO_3$) (Banerjee and Krupanidhi 2012) and thin films of non-magnetic oxides as TiO_2, In_2O_3, and ZnO (Sundaresan and Rao 2009). However, the origin of the magnetism in magnetic materials, as spinel ferrites, is due to the arrangement of the spin moments of the ions in tetrahedral and octahedral sites.

The literature reports various methods to produce magnetic nanoparticles (NPs) such as spinel ferrites (Laurent et al. 2008). Numerous chemical methods can be used: microemulsions (Chin and Yaacob 2007), sol–gel synthesis (Albornoz and Jacobo 2006), sonochemical (Hee Kim et al. 2005), and hydrothermal reactions (Upadhyay et al. 2003). Among these, the hydrothermal synthesis may be the most promising because of its simplicity, productivity, and control of several factors such as size, morphology, and composition (Somiya and Roy 2000). This process is usually conducted at autogenous pressure and single or heterogeneous phase reactions occur in aqueous media to crystallize ceramic materials directly from solution. The hydrothermal crystallization appears greatly beneficial since it offers high control of morphology, size, and agglomeration degree at different working conditions (temperature, time, reactants, and stirring rate) (Suchanek and Riman 2006).

In the last years, a commercial interest in the hydrothermal synthetic approach has been revived due to the accessibility, under mild experimental conditions ($T < 350$ °C, $P < 100$ MPa), of a wide range of different NPs keeping low the costs of their sustainable large scale production. Lee and co-workers (Lee et al. 1999) investigated how, in an hydrothermal process, conditions of temperature and pH may influence the structural and magnetic properties of Ni–Zn ferrite. They observed that, an increased pH (7–10.5) and temperature (180–250 °C) inhibits the formation of the hematite phase (α-Fe_2O_3) and enhances the saturation magnetization (M_s), respectively. On the other hand, the presence in the reaction environment of surfactants and solvents which regulate the NP nucleation and growth, allows to control the NP morphology and size (Suchanek and Riman 2006).

Despite the structural similarity, from the point of view of magnetic properties, the various types of NPs exhibit some distinct differences as a function of their morphology (e.g., spherical, rods, disks, cubes, rhombohedral, tetrapods, or more complex shapes). Alvarez and co-workers (Maia et al. 2008) showed experimentally and through Monte Carlo simulations that the difference in effective shape anisotropy between spherical and cubic geometries of the γ-Fe_2O_3 NPs with similar size leads to substantial differences in the blocking temperature due to the effect of intrinsic magnetocrystalline anisotropy.

In the present study, we report on the synthesis of M–Zn ferrite (M = Ni, Mn) cubic superparamagnetic NPs achieved by a hydrothermal process carried out under mild operative conditions and short reaction times. The structural, morphological, and compositional characterization of the as-obtained NPs have been performed through X-ray diffraction (XRD), Infrared (FTIR), Raman, ^{57}Fe Mössbauer spectroscopy, transmission electron microscopy (TEM) analyses, and magnetic measurements.

Experimental

Materials and methods

All reagents were commercial products with analytical grade without further purification. The chemical reagents for this study are $FeCl_3{\cdot}6H_2O$ (Dinâmica, 97 %) $MnCl_2{\cdot}4H_2O$ (Vetec, 99 %), $NiCl_2{\cdot}6H_2O$ (Vetec, 97 %), $ZnCl_2$ (Dinâmica, 97 %), and sodium hydroxide (Cinética Química, 97 %).

Synthesis of $MZnFe_2O_4$ (M = Mn, Ni) nanoparticles

$MZnFe_2O_4$ nanoparticles were synthesized according to Lee et al. (Lee et al. 1999). Stoichiometrically required amounts of metal chloride were dissolved in a beaker with distilled water. Under vigorous mechanical stirring, an aqueous mixture was prepared with molar ratio 0.5:0.5:2 (M:Zn:Fe). Sodium hydroxide was added into the mixture to precipitate the desired hydroxides. The hydrothermal treatment of the slurry was carried using a Teflon-lined autoclave at 250 °C for 30 min. The reactions occurring during the hydrothermal process can be summarized as follows:

$$0.5M^{2+} + 0.5Zn^{2+} + 2Fe^{3+} + 8OH^{-} \rightarrow Zn_{0.5}M_{0.5}Fe_2O_4 + 4H_2O. \qquad (1)$$

Afterward, the autoclave was cooled to room temperature and the precipitate washed several times by water and methanol. The particles were then dried in air at 100 °C for 3 h. The resultant magnetic NPs were labeled as MnZnFe and NiZnFe respectively. For comparison, MFe_2O_4 NPs were also synthesized (M = Zn, Ni and Mn) and labeled as ZnFe, NiFe, and MnFe, respectively.

Characterization of nanoparticles

X-ray diffraction (XRD)

The X-ray diffraction analysis was obtained using CuKα (1.54056 Å) from X-ray powder diffractometer Riguku with Bragg–Brentano geometry in the range of 20–80°. The phase identification analysis was made by comparing powder diffractograms with standard patterns from International Centre for Diffraction Data. Rietveld refinement procedures (Rietveld 1967) were applied to all diffraction patterns using the DBWS 2.25 (Bleicher et al. 2000), as described by Young and coworkers (Young et al. 1995).

Infrared spectroscopy (FTIR)

The FTIR spectrum was carried out on a Perkin–Elmer Spectrometer in the range 4,000–400 cm^{-1}. In recording IR spectra, each of the samples were mixed with potassium bromide powder and pressed into pellets.

Raman spectroscopy

The Raman spectroscopy was performed using an ALPHA 300 from Witec at room temperature. An 20X objective was used to focus the laser on the sample and to collect the scattered radiation. The laser excitation source was at 532 nm.

^{57}Fe Mössbauer spectroscopy

The Mössbauer spectrum was recorded at room temperature (300 K) from FAST (ConTec) Mössbauer System spectrometer using transmission geometry. A ^{57}Co radioactive source was used. The data analysis was performed using NORMOS program written by R. A. Brand (distributed by Wissenschaftliche Elektronik GmbH, Germany). Isomer shifts (δ) are referred as α-Fe at room temperature.

Magnetization measurements

The magnetization measurements were performed at room temperature with a home-made vibrating sample magnetometer (VSM). The VSM has been previously calibrated using a pure Ni wire, and after measuring the mass of each sample the magnetization was given in emu/g.

Transmission electron microscopy (TEM)

Transmission electron microscopy analysis was performed on a Jeol JEM-1011 electron microscope operating at 100 kV, equipped with a CCD camera ORIUS 831 from Gatan. TEM samples are prepared by drop-casting dilute nanocrystal solutions onto carbon-coated copper grids. Afterward, the deposited samples are allowed to completely dry at 60 °C for one night before examination.

Results and discussion

X-ray diffraction (XRD)

X-ray diffraction patterns and Rietveld refinement data for all synthesized samples are shown in Fig. 1. The diffraction peaks observed in 29.9°, 35.3°, 42.8°, 53.3°, 56.7°, and 62.2° can be indexed to cubic phase (JCPDS

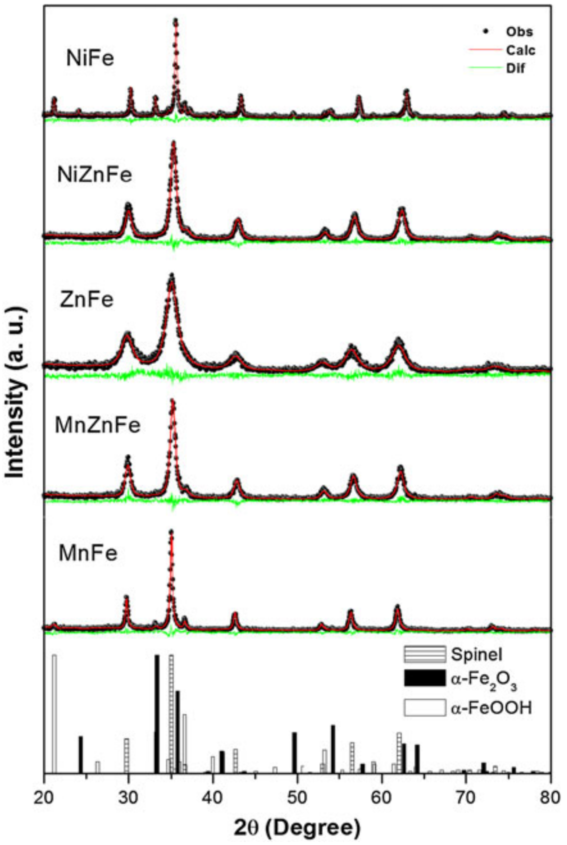

Fig. 1 XRD of the magnetic nanoparticles obtained by hydrothermal synthesis

file n° 086–1355) with symmetry spatial group O_h^7. This phase, which was observed for all the samples, indicated that there was formation of the spinel structure without any calcinations process after synthesis. However, the sample NiFe showed a peak at 33.2°. This indicated the presence of the hematite (α-Fe_2O_3), since this can be attributed to reflections coming from the 104 crystallographic plane (JCPDS file n° 071–0469). For this sample, the α-Fe_2O_3 impurity may be due to the migration of Fe^{3+} out of the spinel structure (Paiva et al. 2008). Moreover, a peak at 21.2° indicates the formation of the goethite (α-FeOOH) (JCPDS file n° 029–0713) for MnFe and NiFe.

The structural data from XRD were treated with DBWTools, version 2.3 program (Bleicher et al. 2000). Table 1 summarizes the data obtained from Rietveld analysis and the main factors (S, R_{wp}, and R_{exp}), which confirm a good refinement. These results suggest that the samples are constituted mainly by spinel phase. NiFe NPs presented peaks relative to α-Fe_2O_3 and α-FeOOH phases, respectively, showing 2.74 and 17.33 % of mass fraction. Only α-FeOOH (1.76 %) was observed for MnFe. It is important to note that in the Rietveld refinement, the most important values to be evaluated were the R_{WP} and S, as they refer to the agreement and the progress of refinement. The literature (Bezerra 2007) report that values in the range 10–20 % for R_{WP} demonstrate the good quality of refinement, while for the S, values <1.3 can be considered satisfactory. The results for these parameters showed in Table 1 evidence the satisfactory character of the refinement.

The extrapolated values of network parameter followed the order: NiFe < NiZnFe < MnZnFe < ZnFe < MnFe. This sequence can be explained considering the ionic radii of the metal constituents of the spinel network which are respectively Ni^{2+} (0.78Å) < Zn^{2+} (0.82 Å) < Mn^{2+} (0.91 Å) (Goldman 2006). Therefore, as expected, the network parameters follow exactly the same order NiFe < ZnFe < MnFe and NiZnFe < MnZnFe.

The particle size was calculated using Scherrer and Willliansom–Hall (W–H) models. The values are displayed in Table 2. It can be noticed that the average particle diameter obtained by Scherrer remain in the range 4.7–25 nm, while for the W–H it was observed 11.5–53.5 nm. It clearly shows the interference of the values microstrain (ε) in the calculation of particle size, since for higher values of ε it was possible to

Table 1 Quantitative phase analysis and crystallographic data obtained from the Rietveld refinement

Samples	Phase fraction in mass (%)			Network parameter (Å)	R_{wp} (%)	S	R_{exp} (%)
	Spinel	α-Fe_2O_3	α-FeOOH				
MnFe	98.24	–	1.76	8.473	20.60	1.13	18.22
MnZnFe	100	–	–	8.426	20.62	1.22	16.93
ZnFe	100	–	–	8.460	16.31	1.02	16.04
NiZnFe	100	–	–	8.411	17.56	1.05	16.67
NiFe	79.94	2.74	17.33	8.343	18.83	1.12	16.79

Table 2 Average crystallite sizes and microstrain percentage obtained by Scherrer and Willianson–Hall (W–H) models

Samples	Average crystallite sizes (D_m) (nm)		Microstrain (ε) (%)
	Scherrer	W–H	
MnFe	18.0	53.5	0.253
MnZnFe	11.2	–	–
ZnFe	4.7	–	–
NiZnFe	10.1	11.5	0.076
NiFe	25.6	37.4	0.090

observe greater discrepancy between the calculated values by Scherrer and W–H.

Vibrational spectroscopy

From the XRD results, it was possible to confirm the presence of spinel phase in all samples. Thus, we carried out a spectroscopic study based on Group Theory in order to predict the number of active bands in FTIR and Raman. To this end, we used nuclear site group analysis developed by Mathew (Porto 1981) and extended to crystals. First of all, it was necessary to know all equivalent sites in the unit cell to determine the symmetry of the lattice modes of the spinel phase with symmetry spatial group O_h^7. According to the literature (Goldman 2006), it was found that this was formed by 32 oxygen atoms forming 64 tetrahedral sites and 32 octahedral sites. However, only 24 are occupied by cations in the network, where 8 tetrahedral and 16 octahedral sites due to considerations of the network load balancing. Table 3 shows that only C_{3v}, T_d, and D_{3d} will accommodate an atomic species within the unit cell. Each nucleus on an O_h^7 site will contribute to a symmetry mode. Then, the lattice modes can now be read directly from Table 4, so the vibrational modes are given by

$$\Gamma = A_{1g} + E_g + T_{1g} + 3T_{2g} + 2A_{2u} + 2E_u + 5T_{1u} + 2T_{2u}. \tag{2}$$

where the T_{1u} modes are FTIR active and $A_{1g} + E_g + 3T_{2g}$ modes are Raman-active. These results are in agreement with literature results (Gupta et al. 2002).

Table 4 Irreducible representations resulting from the occupation of their sites within the space group O_h

Site	Irreducible representations
C_{3v}	$A_{1g} + A_{2u} + E_g + E_u + T_{1g} + 2T_{1u} + 2T_{2g} + T_{2u}$
D_{3d}	$A_{2u} + E_u + 2T_{1u} + T_{2u}$
T_d	$T_{1u} + T_{2g}$

The table show only interesting sites for spinel structure

Figure 2 shows the recorded FTIR spectrum of the nanoparticles in the range 4,000–400 cm^{-1}. As seen previously, there are five normal modes ($5T_{1u}$) infrared lattice vibration. However, the working range is only possible to observe for two modes (Ravinder 1999). It can be seen that the FTIR spectrum are found to exhibit two bands in the range 750–400 cm^{-1}

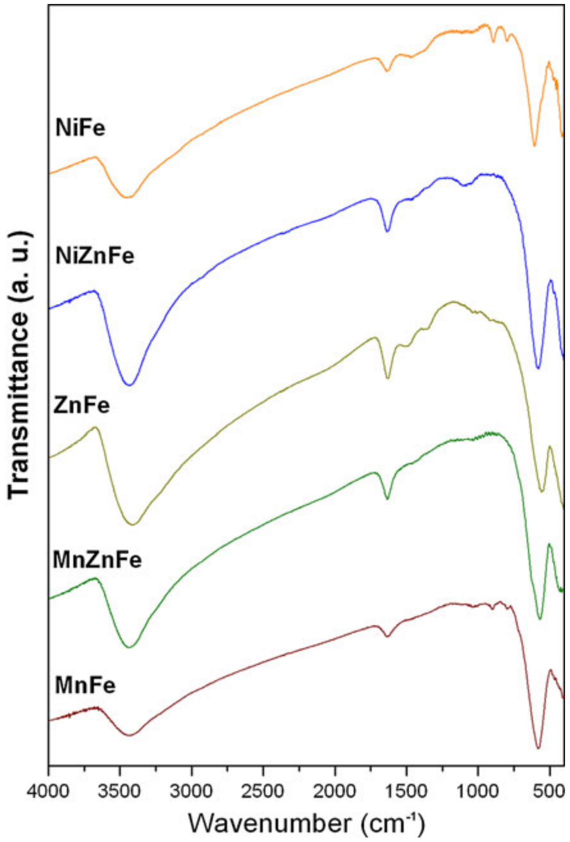

Fig. 2 FTIR for magnetic nanoparticles

Table 3 All sites for the spatial group O_h^7

Spatial Group	Sites
O_h^7 (F4$_1$/m32/m)	$[iC_1(192)] + [hC_2(96)] + [gC_s^d(96)] + [fC_{2v}^d(48) + [eC_{3v}(32)] + (d + c)D_{3d}(16) + (b + a)T_d(8)$

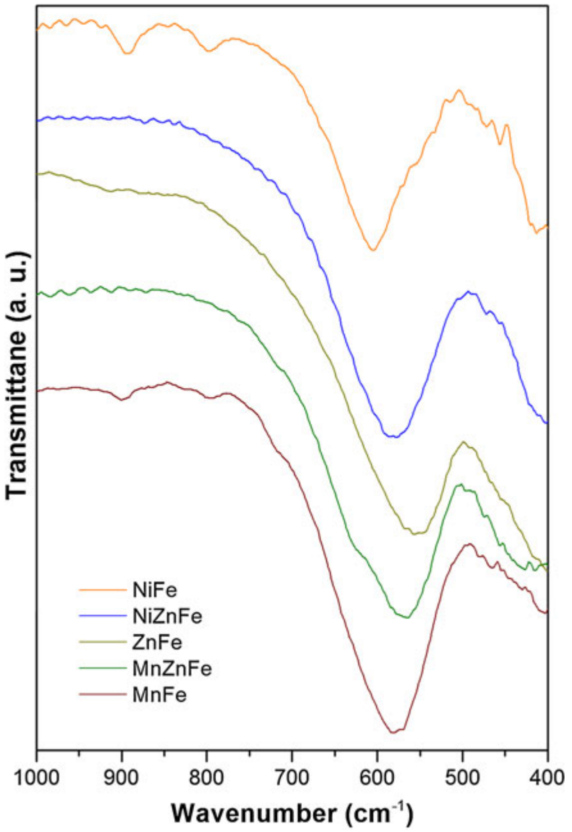

Fig. 3 Band equivalent to the vibration of metal in tetrahedral sites

generally observed for ordered spinel ferrites (Bezerra 2007; Amer et al. 2011). The bands observed in the range 600–550 and 450–385 cm^{-1} can be assigned to the site with symmetry T_d (8*a*) and D_{3d} (16*b*), respectively (Bezerra 2007). However, it is important to mention that "octahedral" sites exhibit a loss of symmetry with a centrosymmetric D_{3d} point group. This fact was similarly observed by Pailhé and co-workers (Pailhé et al. 2008).

The interaction between oxygen and cations in octahedral and tetrahedral positions strongly affects the wavenumber values observed in Fig. 2 (Thomas and George 2009). Thus, the band assigned to the site 8*a* is finer observed because of its better resolution. This band is showed in Fig. 3. It was found that the band positions for MnZnFe and NiZnFe have intermediate values of wavenumbers compared to their

Table 5 Calculated values of force constant (*K*) and frequency (*v*) for all samples synthesized

Sample	*v* (10^{13} Hz)	*K* (10^3 dyne cm^{-1})
MnFe	1.743	246.577
MnZnFe	1.706	239.217
ZnFe	1.659	231.515
NiZnFe	1.737	249.698
NiFe	1.815	268.555

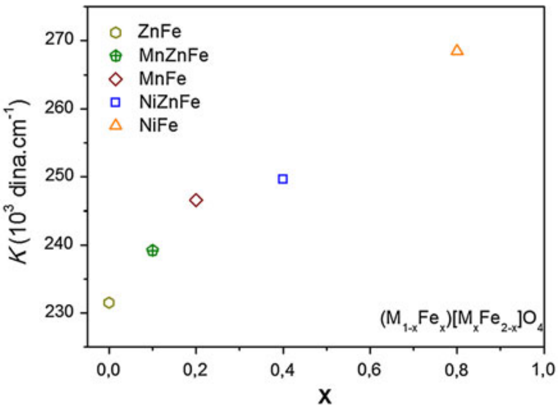

Fig. 4 Values of *K* in function of the amount of Fe^{3+} in tetrahedral site

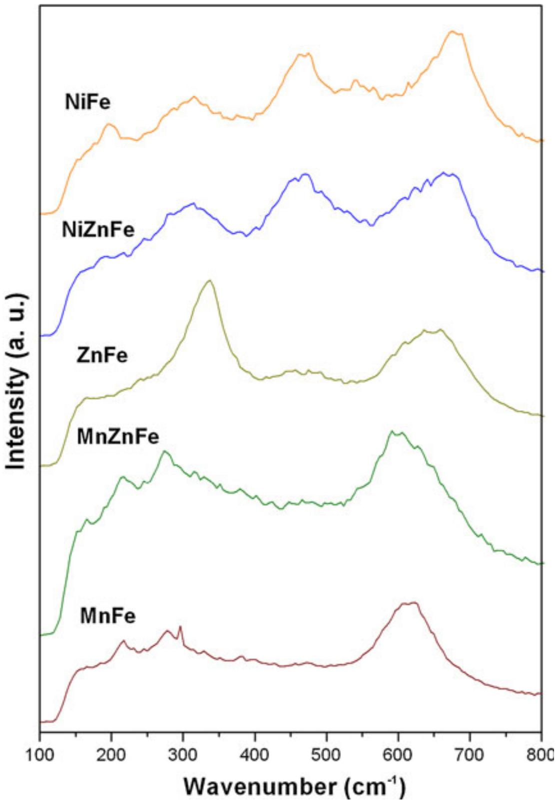

Fig. 5 Raman spectra of the ferrites

respective pure ferrites (MnFe, ZnFe, and NiFe). This can be explained by the fact that cations occupying sites 8*a* influenced the Metal-O interaction. According to the literature (Oliveira 2001), the frequency bands are proportional to a force constant (K), were determined using the relation:

$$v = \frac{1}{2\pi}\sqrt{\frac{K}{\mu}}. \tag{3}$$

where μ is reduced mass and v is frequency. The determined values were listed in Table 5. The values of K were increased as a function of the increase of the amount of Fe^{3+} in tetrahedral site, as we can see in Fig. 4. This can be explained through the bonding nature of Fe^{3+} ions at the tetrahedral sites. Intra-nuclear bond separation of Fe^{3+}–O^{2-} is less leading to the increase bond strength shifting to higher values of K.

The K values for MnZnFe and NiZnFe have intermediates values compared to their respective extremes. Thus, it is expected that the bands position for these samples should appear at intermediate values. In addition, it was possible to identify a shoulder appearing at about 623 cm^{-1} in the sample MnZnFe. The literature

Fig. 6 Mössbauer spectra of the magnetic NPs

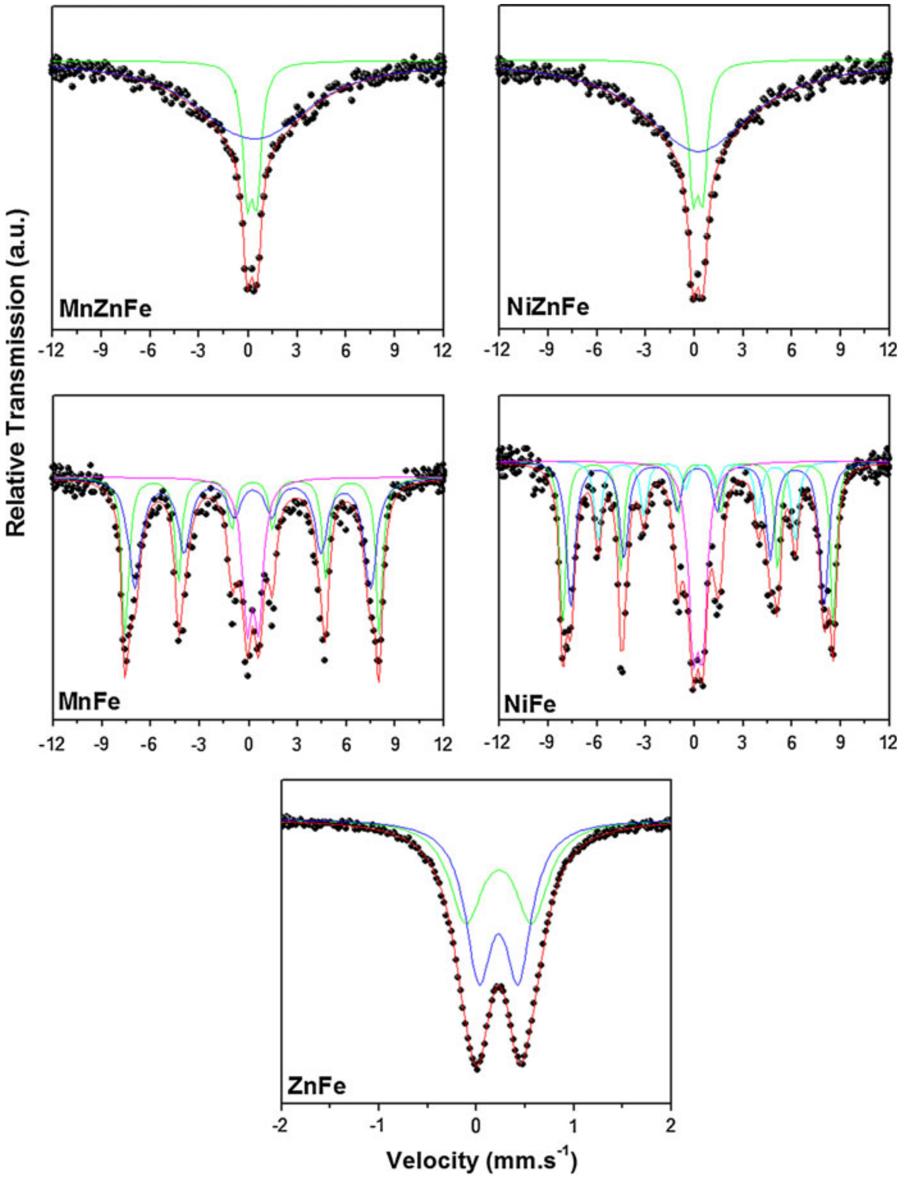

(Dawoud and Shaat 2006; Potakova et al. 1972) reports that the presence of Fe^{2+} ions in the spinel network could cause a local distortion. This produce a non-cubic component with consequent loss of its symmetry properties leading to splits in the shoulders or absorption bands. Thus, we ascribe it to a similar effect due to the presence of Mn^{2+} ions in the spinel network.

The theoretical approach used in this study predicts five Raman-active bands ($A_{1g} + E_g + 3T_{2g}$). However, only the sites T_d and C_{3v} are occupied by M^{n+} and O^{2-} ions, respectively. They contribute to the Raman activity due to the presence of an inversion center in the centrosymmetrical space group O_h^7 (Shebanova and Lazor 2003). Fig. 5 shows the Raman spectrum acquired at room temperature of all samples in the range 180–900 cm^{-1}. Among the predicted vibrational modes for Raman, it is found that only A_{1g} mode was observed for all samples around 600–690 cm^{-1}. This mode is associated to the symmetric stretch of oxygen atoms along M^{n+}–O bonds. In the case of ZnFe, NiZnFe, and NiFe, the spectra clearly exhibit bands in the range 450–500 and 300–350 cm^{-1} assigned at $T_{2g}(3)$ and E_g modes. These can be respectively attributed to symmetric and asymmetric bends of oxygen with respect to M^{n+}. However, NiFe presented weak bands observed at 197 and 544 cm^{-1} attributed to $T_{2g}(1)$ and $T_{2g}(2)$ modes. They correspond to the translatory movement of the whole $M^{n+}O_4$ and asymmetric stretch of Fe and O, respectively. $T_{2g}(1)$ mode was also found for samples MnFe and MnZnFe at 215 cm^{-1}. Interestingly for sample MnFe and MnZnFe, unexpected mode was observed in the range 270–280 cm^{-1}, which could be Raman-active due to the cationic disorder that induces a breakdown of the translation symmetry (Julien and Massot 2003). This is in agreement with the results obtained from FTIR for MnZnFe. It supports that the presence of Mn^{2+} ions in the spinel network causes distortion with consequent loss of their symmetry properties, since the Mn samples showed deviation of ideal spinel structure.

Table 6 Mössbauer parameters for all samples

Samples	Sites	Hyperfine parameters			Area (%)
		δ (mm/s)	Δ (mm/s)	B_{HF} (T)	
NiFe	16*b*	0.28	−0.02	48.3	35.5
	8*a*	0.37	0.07	51.7	27.5
	C_1	0.38	−0.26	37.6	15.5
	D_1	0.31	0.59	–	21.5
NiZnFe	16*b*	–	–	–	80.6
	8*a*	0.32	0.61	–	19.4
ZnFe	16*b*	0.34	0.41	–	54.8
	8*a*	0.34	0.68	–	45.2
MnZnFe	16*b*	–	–	–	79
	8*a*	0.31	0.60	–	21
MnFe	16*b*	0.37	−0.11	44.7	42.1
	8*a*	0.33	0.02	48.3	36.7
	C_2	0.32	0.69	–	21.3

Mössbauer spectroscopy

Figure 6 displays the room temperature Mössbauer spectra of the all samples. The black dots in the figure represent the experimental data, whereas solid red lines coincide with least-square fitting. Moreover, solid lines of different colors indicate the Fe position in several environments. In the case of NiZnFe and MnZnFe, a peak doublet was observed at the centre of the spectra. This pattern can be attributed to the collapse of the magnetic ordering, evidenced as a superparamagnetic character (Wang and Li 2001), which shows a relaxation time (τ) $<\tau_L$ (Larmor precession time of the nuclear magnetic moment) (Malik et al. 2010). This behavior arises from strong influence of thermal energy that occurs with small particle size (Knobel et al. 2008). It was also found a V-shaped for samples NiZnFe and MnZnFe. According to the literature (Upadhyay et al. 2003), the V-shaped can be attributed to several factors such as reduction in magnetocrystalline anisotropy or substitution of nickel and manganese ions with those of zinc weakening the magnetic interactions due to reduction in the A–B coupling pairs. Spectra for sample ZnFe shows a doublet corresponding of a paramagnetic compound indicating the pure Zinc ferrite phase formation (Pailhé et al. 2008). This result is in agreement with the XRD.

Several sub-spectra can be observed in the case of MnFe and NiFe NPs. This effect is indicative of the presence of different magnetic neighbors influencing Fe atoms. In this regard the spectrum of NiFe shows a doublet at the centre along with three sextets patterns. The doublet can be definitely attributed to Fe^{3+} ions inside regions, with so small size particle that exhibit superparamagnetic relaxation phenomenon (Amer et al. 2005). It was found that three sextets correspond to the Fe^{3+} ions in 16*b* and 8*a* sites (ferrite phase) (Pathan et al. 2010) and another site characteristic of the α-FeOOH

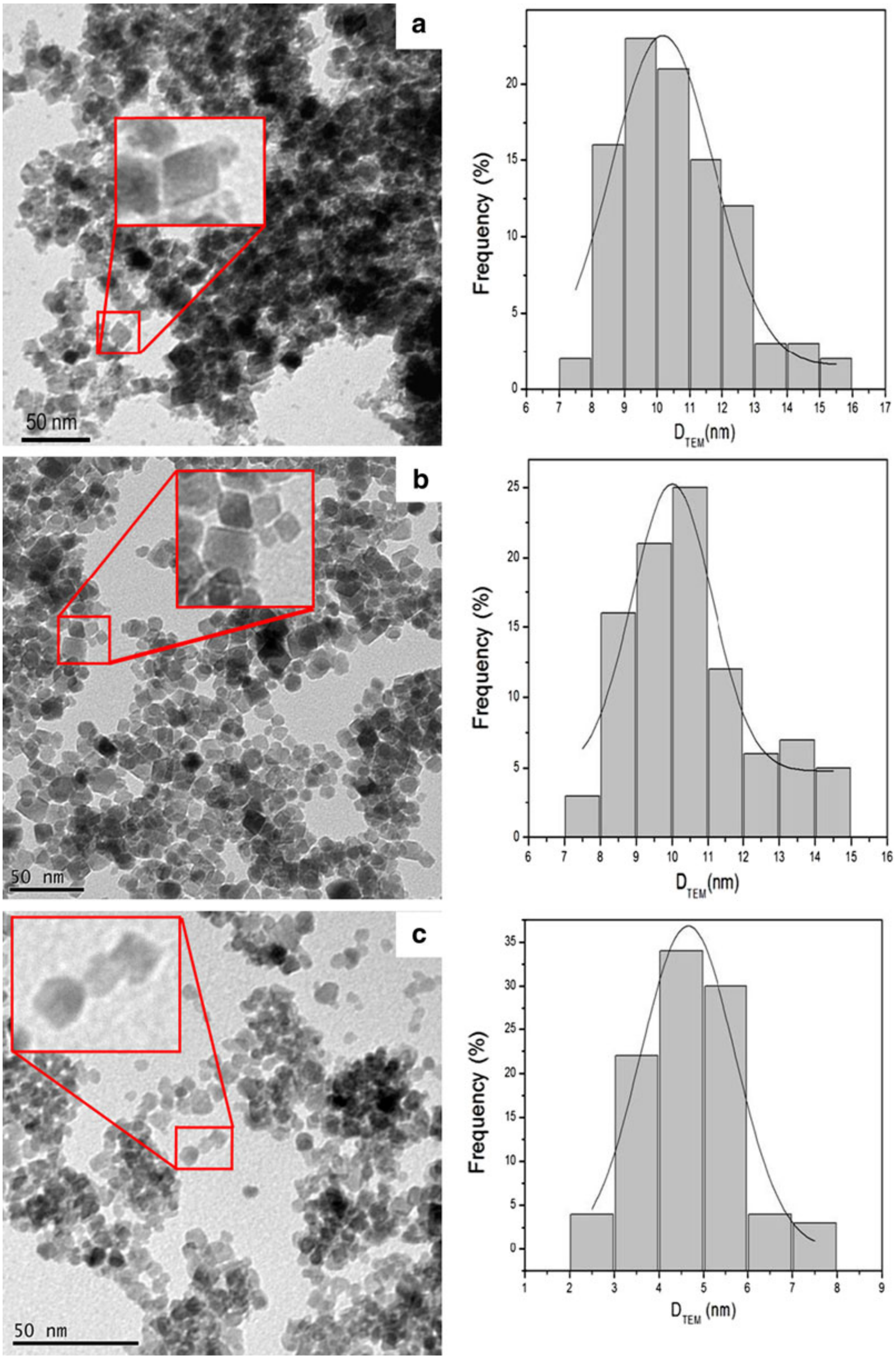

Fig. 7 TEM images respectively of **a** MnZnFe **b** NiZnFe and **c** ZnFe magnetic NPs

phase (Krehula and Musić 2008). Similar results were found for MnFe, however, only two sextets patterns were observed correspondent to the Fe^{3+} ions in 16*b* and 8*a* sites. The sextets pattern characteristic of the α-FeOOH phase was not observed for MnFe. This can be explained by low mass fraction (1.76 %).

Mössbauer hyperfine parameters for all samples are reported in Table 6. For all cases the Fe ion isomeric shift values (δ) remained between 0.28 and 0.38 mm/s. According to literature (Dickson and Berry 1986), values in the range 0.1–0.5 mm/s relative to Fe metal are consistent with the high-spin Fe^{3+} state. A positive shift indicates that the s-electrons density at the nucleus becomes more shielded because of larger number of d-electrons (Gibb 1994; Dickson and Berry 1986). Quadrupole interaction (Δ) has values in the range −0.26–0.69 mm/s. The change of sign may originate from a nonspherical charge distribution at nucleus, which can be positive or negative when elongated or flattened, respectively (Dickson and Berry 1986). The relatively high values of Δ can be assigned to the chemical disorder and the local symmetry reduction in site (Singhal et al. 2006).

Transmission electron microscopy (TEM)

Figure 7 shows TEM images of the samples MnZnFe (a), NiZnFe (b), and ZnFe (c) as well as the size distributions aside. The size distribution was determined by measurement of 100 randomly selected particles in different regions of the expanding TEM images. It is worthwhile to note that the nanoparticles are almost cubic in shape with an average diameter about 12 ± 3, 10 ± 2, and 5 ± 1 nm for MnZnFe, NiZnFe, and ZnFe, respectively. This result was in accordance with that of XRD.

Magnetization measurements

The vibrating sample magnetometer analysis was performed to investigate the NPs magnetic properties at room temperature. In Fig. 8, the hysteresis loops characteristic of a superparamagnetic behavior can be observed for all samples. There is no hysteresis in the magnetization curves for the samples with the presence of Zn, with both remanence and coercivity being zero, indicating that these magnetic NPs are superparamagnetic. The sample ZnFe was not saturated in the field range used, thus indicating the possible presence of paramagnetic NPs, or very fine superparamagnetic NPs. In the samples MnFe and NiFe, it was observed a small coercivity around 70 Oe reasonably due to the presence of larger NPs in these samples.

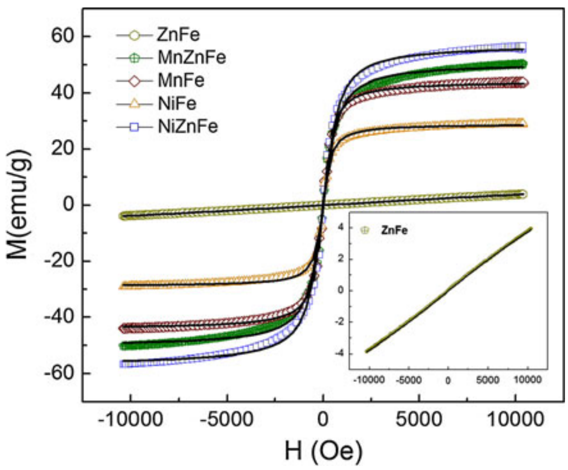

Fig. 8 Magnetization curves of the samples. As discussed in the text, the data have been fitted (*solid lines*) through a Langevin function

The hysteresis curves at room temperature of these samples can be well-described by a Langevin function (Barreto et al. 2011),

$$\frac{M}{Mo} = \coth\left(\frac{mH}{K_B T}\right) - \frac{K_B T}{mH}. \tag{4}$$

where m is the magnetic moment, H is the external magnetic field, T is the temperature, and k_B is the Boltzmann constant. In Fig. 7, the solid lines are the best fitting curves obtained with the Langevin function for each sample. The particle sizes can be inferred from this Langevin function adjusting the parameter $a = \mu/k_b$ which is related to the diameter of the particle as $a = 4\pi(d/2)^3 M_0/3k_B$ with d being the diameter of the particle. Thus, using this function to fit the curves we obtain the average diameter of the nanoparticles that is shown in Table 7. These results agree with the sizes determined from XRD for MnZnFe, ZnFe, and NiZnFe, as can be seen from Tables 2 and 5. In the case of NiFe and MnFe the Langevin function cannot be accurately used due to the small coercivity existing in these samples, therefore the sizes obtained by the fitting of the magnetization curves are smaller than those obtained by XRD.

Table 7 Calculated values of the average diameter of the nanoparticles obtained from the fit using the Langevin function

Sample	*D* (nm)
MnFe	12.6
MnZnFe	10.6
ZnFe	5.5
NiZnFe	10.1
NiFe	15.5

Conclusions

The synthesis of cubic superparamagnetic $MZnFe_2O_4$ (M = Mn or Ni) NPs has been performed according to hydrothermal process along with a co-precipitation approach without any procedure of calcination. Particles size of mixed ferrites presented a range 4.7–25 nm when calculated using Scherrer and Langevin methodology. Whereas following a Willinason-Hall procedure it was found 11.5–56.8 nm due to the correction factor from NPs microstrain. Transmission electron microscopy confirms that the NPs have average diameters (5–12 nm) in the range of those obtained from XRD technique. The absorption bands, predicted by spectroscopic analysis based on the Group Theory, were observed by FTIR and Raman investigations. A superparamagnetic behavior was observed by Mössbauer spectroscopy and studies of magnetic hysteresis. This kind of material can be used as precursor in drug delivery systems, magnetic hyperthermia, ferrofluids or magnetic imaging contrast agents.

Acknowledgments This study was supported by CAPES, Funcap, and CNPq (Brazilian agencies). The support from Fondecyt 1110252; Millennium Science Nucleus, Basic and Applied Magnetism Grant N°P10-061-F and CONICYT BASAL CEDENNA FB0807, are gratefully acknowledged. L. Carbone acknowledges financial support by the Italian Ministry of Education, University and Research through the project AEROCOMP (contract MIUR no. DM48391). L. Carbone performed TEM investigations c/o the Istituto Nanoscienze –CNR NNL UOS Lecce.

References

Albornoz C, Jacobo SE (2006) Preparation of a biocompatible magnetic film from an aqueous ferrofluid. J Magn Magn Mater 305(1):12–15

Amer MA, Meaz TM, Ata-Allah S, Aboul-Enein S, Abd-El-Hamid MO (2005) Mössbauer, infrared and X-ray Studies of $Ni_{0.5}Zn_{0.5}Cr_xFe_{2-x}O_4$ ferrites. Egypt J Solids 28:3

Amer MA, Tawfik A, Mostafa AG, El-Shora AF, Zaki SM (2011) Spectral studies of Co substituted Ni–Zn ferrites. J Magn Magn Mater 323(11):1445–1452

Banerjee N, Krupanidhi SB (2012) Anomalous magnetic behavior of La0.6Sr0.4MnO3 nano-tubes constituted with 3–12 nm particles. Appl Phys A:1–8. doi: 10.1007/s00339-012-7272-0

Barreto A, Santiago V, Mazzetto S, Denardin J, Lavín R, Mele G, Ribeiro M, Vieira I, Gonçalves T, Ricardo N, Fechine P (2011) Magnetic nanoparticles for a new drug delivery system to control quercetin releasing for cancer chemotherapy. J Nanopart Res 13(12):6545–6553

Bezerra MJOS (2007) Síntese e Caracterização da ferrita de MnZn obtida pelo método dos citratos precursores Universidade Federal do Rio Grande do Norte, Natal

Bleicher L, Sasaki JM, Paiva Santos CO (2000) Development of a graphical interface for the Rietveld refinement program DBWS. J Appl Crystallogr 33(4):1189

Chin AB, Yaacob II (2007) Synthesis and characterization of magnetic iron oxide nanoparticles via w/o microemulsion and Massart's procedure. J Mater Process Technol 191(1–3):235–237

Daniels JM, Rosencwaig A (1970) Mossbauer study of the Ni–Zn ferrite system. Can J Phys 48(4):381–396

Date SK, Joy PA, Kumar PSA, Sahoo B, Keune W (2004) Structural, magnetic and Mössbauer studies on nickel–zinc ferrites synthesized via a precipitation route. Phys Status Solidi (C) 1(12):3495–3498

Dawoud HA, Shaat SK (2006) A structural study of Cu–Zn ferrites by infrared spectra. Al-aqsa J 10:247–262

Dickson DPE, Berry FJ (1986) Mössbauer spectroscopy. Cambridge University Press, USA

Gibb TC (1994) Encyclopedia of Inorganic Chemistry. Jonh Wiley and Sons, Chidrester

Goldman A (2006) Modem Ferrite Technology. Springer, Pittsburgh

Gupta R, Sood AK, Metcalf P, Honig JM (2002) Raman study of stoichiometric and Zn-doped Fe_3O_4. Phys Rev B 65(10):104430

Hee Kim E, Sook Lee H, Kook Kwak B, Kim B-K (2005) Synthesis of ferrofluid with magnetic nanoparticles by sonochemical method for MRI contrast agent. J Magn Magn Mater 289:328–330

Julien CM, Massot M (2003) Raman spectroscopic studies of lithium manganates with spinel structure. J Phys Condens Matter 15(19):3151

Knobel M, Nunes WC, Socolovsky LM, De Biasi E, Vargas JM, Denardin JC (2008) Superparamagnetism and other magnetic features in granular materials: a review on ideal and real systems. J Nanosci Nanotechnol 8:2836–2857

Krehula S, Musić S (2008) Influence of cobalt ions on the precipitation of goethite in highly alkaline media. Clay Miner 43:95–105

Laurent S, Forge D, Port M, Roch A, Robic C, Vander Elst L, Muller RN (2008) ChemInform abstract: Magnetic iron oxide nanoparticles: synthesis, stabilization, vectorization, physicochemical characterizations, and biological applications. ChemInform 39 (35):no–no

Lee JH, Maeng DY, Kim YS, Won CW (1999) The characteristics of Ni–Zn ferrite powder prepared by the hydrothermal process. J Mater Sci Lett 18(13):1029–1031

Leung LK, Evans BJ, Morrish AH (1973) Low-temperature Mossbauer study of a Nickel–Zinc ferrite: $Zn_xNi_{1-x}Fe_2O_4$. Phys Rev B 8(1):29–43

Maia DF, Dantas BB, Dias G, Freitas NL, Costa ACFM (2008) Influência dotipo de combustível na síntese por reação e combustão do catalisador ZnAl2O4. In: 18 CBECiMat—Congresso Brasileiro de Engenharia e Ciências dos Materiais, Porto de Galinhas

Malik R, Annapoorni S, Lamba S, Raghavendra Reddy V, Gupta A, Sharma P, Inoue A (2010) Mossbauer and magnetic studies in nickel ferrite nanoparticles: effect of size distribution. J Magn Magn Mater 322(23):3742–3747

Oliveira LFC (2001) Espectroscopia molecular. Química Nova na Escola 4:24–30

Pailhé N, Wattiaux A, Gaudon M, Demourgues A (2008) Correlation between structural features and vis-NIR spectra of α-Fe2O3 hematite and AFe2O4 spinel oxides (A = Mg, Zn). J Solid State Chem 181(5):1040–1047

Paiva ACLA, Silva VJ, Vieira DA, Gama L, Costa ACFM (2008) Síntese e caracterização de pós de ferrita Mn–Zn: efeito da substituição do Mn^{2+} pelo Fe^{2+} e da quantidade de H_2O. Revista Eletrônica de Materiais e Processos 3(1):25–30

Pathan AN, Kalyani S, Pangal AAG (2010) Synthesis and Mössbauer studies on Nickel–Zinc–Copper nanoferrites. Nanotechnol Nanosci 1(1):13–16

Porto S (1981) Normal mode determination in crystals. J Raman Spectrosc 10:253–290

Potakova VA, Zverev ND, Romanov VP (1972) On the cation distribution in $Ni_{x-y}Fe_x^{2+}Zn_yFe_2{}^{3+}O_4$ spinel ferrites. Phys Status Solidi (a) 12(2):623–627

Ravinder D (1999) Far-infrared spectral studies of mixed lithium–zinc ferrites. Mater Lett 40(5):205–208

Rietveld HM (1967) Line profiles of neutron powder-diffraction peaks for structure refinement. Acta Cryst 22:151–152

Shebanova ON, Lazor P (2003) Raman spectroscopic study of magnetite ($FeFe_2O_4$): a new assignment for the vibrational spectrum. J Solid State Chem 174(2):424–430

Siddique M, Butt NM (2010) Effect of particle size on degree of inversion in ferrites investigated by Mossbauer spectroscopy. Phys B 405(19):4211–4215

Singhal S, Barthwal SK, Chandra K (2006) Structural, magnetic and Mossbauer spectral studies of nanosize aluminum substituted nickel zinc ferrites. J Magn Magn Mater 296(2):94–103

Somiya S, Roy R (2000) Hydrothermal synthesis of fine oxide powders. Bull Mater Sci 23:453–460

Suchanek WL, Riman RE (2006) Hydrothermal synthesis of advanced ceramic powders. Adv Sci Technol 45:184–193

Sundaresan A, Rao CNR (2009) Implications and consequences of ferromagnetism universally exhibited by inorganic nanoparticles. Solid State Commun 149(29–30):1197–1200

Thomas M, George KC (2009) Infrared and magnetic study of nanophase zinc ferrite. Indian J Pure Ap Phys 47:81–86

Upadhyay C, Mishra D, Verma HC, Anand S, Das RP (2003) Effect of preparation conditions on formation of nanophase Ni–Zn ferrites through hydrothermal technique. J Magn Magn Mater 260 (1â€"2):188–194

Vucinic-Vasic M, Antic B, Kremenovic A, Nikolic AS, Stoiljkovic M, Bibic N, Spasojevic V, Colomban P (2006) Zn,Ni ferrite/NiO nanocomposite powder obtained from acetylacetonato complexes

Wang L, Li FS (2001) Mossbauer study of nanocrystalline Ni–Zn ferrite. J Magn Magn Mater 223(3):233–237

Young RA, Sakthivel A, Moss TS, Paiva-Santos CO (1995) DBWS-9411—an upgrade of the DBWS*.* programs for Rietveld refinement with PC and mainframe computers. J Appl Crystallogr 28(3):366–367. doi:10.1107/S0021889895002160